

Solitons in Arbitrary Dimensions Stabilized by Photon-Mediated Interactions

Haoqing Zhang^{1,2}, Anjun Chu^{1,2}, Chengyi Luo¹, James K. Thompson¹, and Ana Maria Rey^{1,2}

¹*JILA, NIST and Department of Physics, University of Colorado, Boulder, Colorado 80309, USA*

²*Center for Theory of Quantum Matter, University of Colorado, Boulder, Colorado 80309, USA*

(Received 29 April 2025; accepted 16 September 2025; published 21 October 2025)

We propose a scheme to generate solitons in arbitrary dimensions, in a matter-wave interferometer, without the need of quantum degeneracy. In our setting, solitons emerge by balancing the single-particle dispersion with engineered cavity-mediated exchange interactions between two wave packets, which, at the appropriate conditions, remain bound to each other and dispersion-free. For detection in thermal gases, we propose an interferometric probing scheme instead of traditional time-of-flight imaging.

DOI: 10.1103/qrk6-phhk

Introduction—Solitons, or self-enforcing waves that propagate without spreading, are a hallmark of nonlinear physics across diverse systems, from water waves to optical pulses in fibers. The realization of Bose-Einstein condensation (BEC) in weakly interacting atomic gases opened avenues for exploring quasi-one-dimensional (1D) matter-wave solitons and nonlinear phenomena [1–5]. In higher dimensions (2D and 3D), stable soliton formation is more complicated, due to dynamical or thermodynamical instabilities and interaction-induced collapse. Only recently have stable bright 2D solitons been realized [6,7].

Atomic solitons have also been identified as promising candidates for inertial sensing, due to their dispersionless character over long integration times and reduced spatial inhomogeneities during pulse sequences [8–15]. However, the need to prepare atoms in a BEC imposes practical limits for sensing tasks.

Here we propose generating solitons in thermal atoms, and in arbitrary dimensions via exchange interactions between momentum states in an optical cavity. We use exchange interactions to open a gap in the many-body spectrum to protect spin alignment and suppress against single-particle inhomogeneity [16–24], as reported in prior work [20], but in addition, we demonstrate that, for specific values of the exchange interaction energy, cavity-mediated interactions can also prevent atomic dispersion and lead to a soliton made of two overlapped wave packets.

Our implementation has some similarities to theoretical ideas based on spin-orbit coupling (SOC) [25–28] to stabilize solitons with contact interactions in 2D [29] and 3D [30] systems, but which exhibit several distinctive features: our solitons possess fringes that depend on the coherence between different momentum states; they do not require a BEC and can emerge in a thermal gas; and they can manifest in 1D, 2D, and 3D systems. Furthermore, the same exchange interactions that generate the solitons can entangle the momentum states, enabling applications to quantum-enhanced interferometry [31].

Model—We consider the experimental setup recently implemented in Refs. [20,32,33] and shown in Fig. 1(a). In this setting, an ensemble of N_0 laser-cooled ^{87}Rb atoms with mass M is placed inside a vertical optical cavity along the \hat{z} direction. The initial thermal distribution of the motional degrees of freedom can be described by the Wigner function $f(\mathbf{r}, \mathbf{p}) \propto e^{-\beta((\mathbf{p}^2/2M)+U(\mathbf{r}))}$ with a characteristic thermal width $\sigma_T = \sqrt{\beta/(M\omega^2)}$, where $\beta = 1/k_B T$ is the inverse temperature. $U(\mathbf{r})$ is the 3D trapping potential

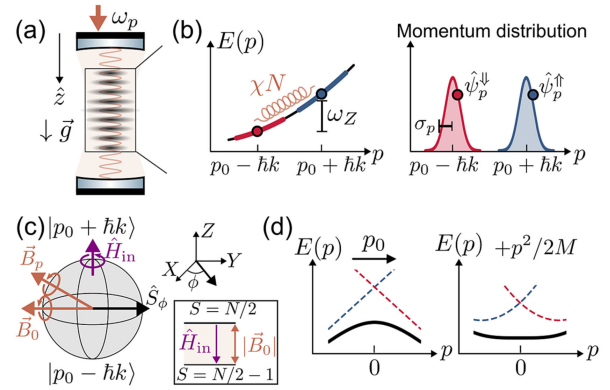


FIG. 1. (a) Schematic of the interferometry protocol in a cavity. (b) Cavity-mediated interactions between atoms in the two wave packets, each with average momentum $p_0 - \hbar k$ and $p_0 + \hbar k$, momentum spread σ_p , and separated by an energy difference ω_Z , create an energy gap, χN , which keeps the wave packets bound. (c) At the mean-field level, for $\chi < 0$, the Bloch vector of an individual atom [initially pointing on the equator along an initial angle ϕ , \hat{S}_ϕ (black arrow)] precesses around the effective magnetic field (orange arrows) $\vec{B}_p = \vec{B}_0 + 2k p_r / M \hat{z}$, with contributions from the self-generated field and kinetic energy (purple) and with $\vec{B}_0 = \chi N \hat{S}_\phi$. (d) At the optimal interaction strength, in a frame moving with momentum p_0 , the modified Doppler dispersion by the exchange interactions plus the free dispersion (dashed lines) generates a net flat dispersion (black solid line), enabling the formation of a soliton.

energy. The trap along \hat{z} is then released, allowing atoms to fall freely under the gravitational acceleration, \vec{g} , with the only confinement along radial direction R and prepared in a well-defined momentum state $(p_0 - \hbar k)\hat{z}$ via velocity selection, without changing the atom's internal quantum state. Here, $k = 2\pi/\lambda$ and $\lambda = 780$ nm for Rb atoms [20,32,33]. This process transforms the Wigner function for the N selected atoms into $\tilde{f}(\mathbf{r}, \mathbf{p}) \propto e^{-(p-(p_0-\hbar k))^2/2\sigma_p^2} \tilde{F}(z, R, p_R)$, featuring a much narrower momentum spread $\sigma_p \ll \hbar k \ll \sigma_T$ along \hat{z} . Here, \tilde{F} describes the part of the Wigner function that depends on the remaining degrees of freedom.

A two-photon Bragg transition, applied after the momentum selection, coherently couples an atom in momentum $|p - \hbar k\rangle$ to another momentum state $|p + \hbar k\rangle$ within the same internal level, enabling the preparation of arbitrary coherent superpositions $[\hat{\psi}_{p-\hbar k} \rightarrow \cos(\theta/2)\hat{\psi}_{p-\hbar k} + \sin(\theta/2)\hat{\psi}_{p+\hbar k}]$, which generate a density grating in position space [Fig. 1(a)]. Here we have defined $\hat{\psi}_{p-\hbar k}$ to be the annihilation momentum operator of a particle with momentum $p - \hbar k$, and θ is the pulse area.

Cavity-mediated interactions between momentum states can be generated by driving the cavity with a laser with frequency ω_p , detuned from the atomic transition—with frequency ω_a —by $\Delta_a = \omega_a - \omega_p$, and from the cavity resonance, ω_c , by $\Delta_c = \omega_c - \omega_p$. By adiabatically eliminating the atomic excited state and the cavity field, one can obtain an effective Hamiltonian within the ground-state manifold that governs only the motional degrees of freedom [20,34,35].

For simplicity, we will assume a single realization of the experiment, in which the selected atoms, before the Bragg pulse, occupy a set of momentum states which we label as $\{p_1, p_2, \dots, p_N\}$, where p_r describes a particle with the momentum $p_0 - \hbar k + p_r$ sample from the Wigner function, $\tilde{f}(\mathbf{r}, \mathbf{p})$. The initialization protocol allows us to focus on momentum states within the region $[p_0 - 2\hbar k, p_0 + 2\hbar k]$. In a frame moving with momentum p_0 , we define the basis states $|\downarrow_p\rangle_n \equiv |p - \hbar k\rangle_n$ and $|\uparrow_p\rangle_n \equiv |p + \hbar k\rangle_n$ for $p \in [-\hbar k, \hbar k]$, and we introduce the pseudospin-1/2 operator $\hat{s}_{p_n}^\eta = \sum_{\alpha, \beta = \uparrow, \downarrow} (\hat{\psi}_{p_n}^\alpha)^\dagger \sigma_{\alpha, \beta}^\eta \hat{\psi}_{p_n}^\beta / 2$ ($\eta = X, Y, Z$), where $\sigma_{\alpha, \beta}^\eta$ are the Pauli matrices and $\hat{\psi}_{p_n}^\alpha$ is the annihilation operator of an atom [Fig. 1(b)], with momentum state $|\alpha_p\rangle_n$. The Hamiltonian then reduces to

$$\hat{H} = \hat{H}_{\text{ex}} + \hbar\omega_Z \hat{S}_Z + \hat{H}_{\text{in}}, \quad \hat{H}_{\text{ex}}/\hbar = \chi \hat{S}_+ \hat{S}_-, \quad (1)$$

with the collective spin observables defined as $\hat{S}_\eta = \sum_{r=1}^N \hat{s}_{p_r}^\eta$. The first term describes the exchange interaction $\chi \hat{S}_+ \hat{S}_- = \chi(\hat{S}^2 - \hat{S}_Z^2 + \hat{S}_Z)$, and the second term accounts for the average kinetic energy difference between the momentum states $p_0 + p_r \pm \hbar k$ and $\omega_Z = 2\hbar k p_0 / M$ [Fig. 1(b)]. The third term, $\hat{H}_{\text{in}} = \hat{H}_{\text{in}}^d + \hat{H}_{\text{in}}^c$, has two

contributions. $\hat{H}_{\text{in}}^d/\hbar = \sum_{r=1}^N (2k p_r / M) \hat{s}_{p_r}^Z$ is the pseudo-spin-dependent single-particle kinetic energy. It induces a differential phase for each momentum pseudospin, and it generates a net spatial separation between the wave packets, each one moving with momentum $\pm \hbar k$, resulting in loss of coherence. $\hat{H}_{\text{in}}^c/\hbar = \sum_{r=1}^N (p_r^2 / 2M\hbar) \hat{I}_{p_r}$ is the spin-independent single-particle dispersion. It imparts a global phase that is identical for both the $|\downarrow_{p_r}\rangle$ and $|\uparrow_{p_r}\rangle$ states but varies with p_r , and it causes the position-space wave packets to spread with time. $\hat{I}_{p_r} = (\hat{\psi}_{p_r}^\uparrow)^\dagger \hat{\psi}_{p_r}^\uparrow + (\hat{\psi}_{p_r}^\downarrow)^\dagger \hat{\psi}_{p_r}^\downarrow$ is the momentum-number operator and a constant of motion in our system. While the spin coherence can be restored by the application of a spin-echo pulse in the middle of the evolution, the ballistic expansion of each of the wave packets in position space induced by \hat{H}_{in}^c cannot be restored.

The exchange interaction term does not commute with \hat{H}_{in} , and it can be used to suppress both wave-packet separation and broadening thanks to the term \hat{S}^2 in \hat{H}_{ex} , which creates a many-body gap, χN [inset of Fig. 1(c)], between the fully symmetric Dicke manifold ($S = N/2$) and the lower symmetry states ($S = N/2 - 1$) [16–21]. The gap favors spin alignment and acts like a spring connecting the two wave packets, preventing their separation while simultaneously extending the system's coherence [20].

Mean-field dynamics—The suppression of the wave-packet broadening can be illustrated for an initial state where all atoms are aligned along the X direction ($\theta = \pi/2$). Under the mean-field approximation, the Hamiltonian, in a frame rotating at ω_Z , reduces to $\hat{H}_{\text{MF}} = \hbar \sum_r \vec{B}_{p_r} \cdot \vec{s}_{p_r} + \hat{H}_{\text{in}}^c$ with $\vec{B}_{p_r} = \{\chi N, 0, (2k p_r / M)\}$. In the regime where $|\chi|N \gg 2k\sigma_p/M$ (we set $\chi < 0$), the relevant eigenvalues take the form

$$E_{p_r} \approx -\frac{1}{2} |\vec{B}_{p_r}| + \frac{p_r^2}{2M\hbar} \approx \frac{\chi N}{2} + \left(1 + \frac{4E_R}{\chi N}\right) \frac{p_r^2}{2M\hbar}, \quad (2)$$

where $E_R = \hbar k^2 / 2M$ is the recoil energy. Note that such a type of dispersion emulates the dynamics of a relativistic particle, and it has been realized with a single trapped ion [36] or in BECs subject to spin-orbit coupling [37]. In our case, Eq. (2) describes a particle with a rest-mass energy $M^* = M / (1 + 4E_R / \chi N)$ and an effective speed of light $c_s = \sqrt{N |\chi / 2M^*|}$. When

$$N\chi_{\text{opt}} = -4E_R, \quad (3)$$

$M^* \rightarrow \infty$ and results in a flattened dispersion [right panel of Fig. 1(d)]. Consequently, at χ_{opt} the wave packets propagate as a soliton, which features no dispersion. Even though the optimal $\chi_{\text{opt}} N$ exceeds the current value used in Ref. [20], the difference is only a factor of 5. The optimal value is attainable by the use of a higher atom number

and/or stronger laser power. We emphasize that similar flattening of the band can be realized for noninteracting atoms with an additional driving field along the X axis with Rabi frequency $\Omega = 4E_R$. However, due to the $U(1)$ symmetry of the exchange interaction, a soliton stabilized by the self-generated field can exist regardless of the initial orientation of the collective spin in the X - Y plane [see Fig. 1(c) for the arbitrary initial state on the equator]. As a result, the protection will not be canceled by a spin echo pulse.

While so far we have focused on $\theta = \pi/2$, solitons can also be engineered for any θ , as shown in Fig. 3(a). The only difference is that in this case, there is an additional Ising term in the exchange interactions $-\chi\hat{S}_Z^2$, which at the mean-field level changes $\vec{B}_{p_r} \rightarrow \{\chi N, 0, (2kp_r/M) - \chi N \cos \theta\}$. The latter generates a net precession that needs to be accounted for. As detailed in the SM [38], the optimal interaction strength is given by

$$\chi_{\text{opt}}(\theta) = \chi_{\text{opt}} \sin^2 \theta \quad (4)$$

with a modified average momentum $p_0 - \hbar k \cos \theta$. Notably, the optimal interaction strength decreases as the initial state approaches either the north or south poles. However, the condition $|\chi_{\text{opt}}(\theta)|N \gg 2k\sigma_p/M$ needs to be enforced at all times, a requirement that significantly reduces the allowed σ_p in the vicinity of the poles.

The wave-packet dynamics can be simulated using the mean-field equations of motion [38], with results shown in Fig. 2. We only show a single realization to facilitate visualization. The thermal average needs to be realized by sampling over the Wigner function. For a free particle with $\chi = 0$ [Fig. 2(a)], the two sampled wave packets separate and broaden over time. In contrast, the wave packets remain bound to each other for $\chi = \pm\chi_{\text{opt}}$, as shown in Figs. 2(b) and 2(c). At the optimal interaction strength $\chi = \chi_{\text{opt}}$

[Fig. 2(b)], the wave packets maintain their initial shape during propagation, generating a soliton. On the other hand, for $\chi = -\chi_{\text{opt}}$ [Fig. 2(c)], the wave packets not only broaden over time but even deviate from their Gaussian profiles at later times.

The evolution of the wave packets is quantitatively analyzed in Fig. 2(d), where we track the rms width in position space $\sigma_z(t_d)$ by fitting the wave packets as Gaussian functions over time t_d . The ratio of the rms width to its initial value is plotted as a function of time. For $\chi = \chi_{\text{opt}}$, the rms width remains constant over an extended period, when the soliton is formed. In contrast, the free evolution case exhibits typical diffusion dynamics, while for $\chi = -\chi_{\text{opt}}$, the wave packets broaden more than the free evolution case.

Figure 3(b) shows the ratio between the fitted rms width σ_z^* after a long evolution time and the initial width for different initial polar angles θ . The solutions confirm that the optimal exchange interaction strength follows Eq. (4) (black dashed line). Furthermore, Fig. 3(c) reveals that the soliton is robust and persists over a broad range of interaction strengths around the predicted optimal value (red solid line). The robustness is stronger close to the equator, where $\chi_{\text{opt}}(\theta)$ reaches a maximum. As a final remark, we note that while the Gaussian wave packet is not an exact soliton solution, it is nevertheless a very good approximation; higher-order terms in momentum p , which we neglected in our analysis can cause broadening at longer timescales. Numerical simulations nevertheless confirm that these corrections are quite small. On the contrary, quantum fluctuations neglected so far can lead to soliton collapse.

Solitons in 2D and 3D—The above mechanism can be generalized to a 2D system by adding a drive perpendicular to the cavity axis, as shown in Fig. 4(a). In this case, one needs to first start with atoms in internal state $|\downarrow\rangle$, and with momentum centered around zero $\vec{p}_0 = (0, 0)$ by velocity selection. The momentum being zero relative to the frame

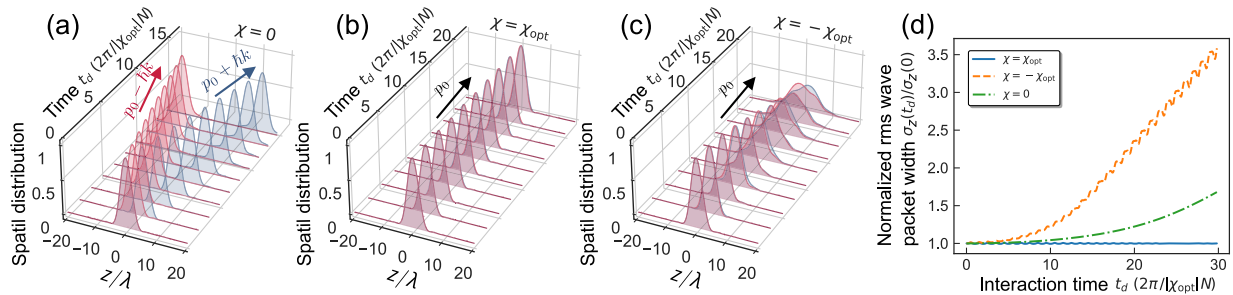


FIG. 2. Mean-field simulation of the soliton dynamics, for a given experimental realization sampled from the Wigner function. We show the separate evolution of the density distribution of each wave packet, ignoring interference terms. After a $\pi/2$ Bragg pulse, the $p_0 - \hbar k$ (red) and $p_0 + \hbar k$ (blue) wave packets spatially propagate according to three scenarios: (a) If $\chi = 0$, the wave packets spatially separate while broadening over time as free particles. (b) If $\chi = \chi_{\text{opt}}$, the wave packets merge and maintain their shape, demonstrating soliton behavior. (c) If $\chi = -\chi_{\text{opt}}$, the wave packets merge but show enhanced broadening compared to the free evolution case. (d) Time evolution of the rms width of the spatial profile (using a Gaussian fit), normalized by the initial width. For $\chi = \chi_{\text{opt}}$, the broadening is suppressed, consistent with the formation of a soliton.

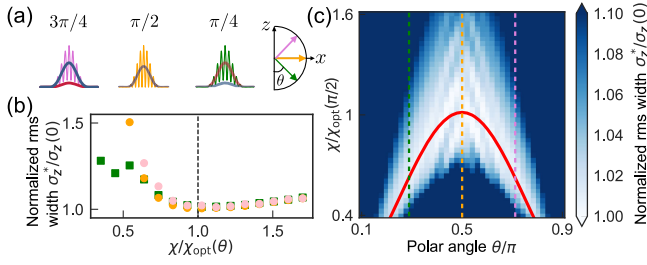


FIG. 3. Wave-packet dynamics for arbitrary polar angle θ using mean-field simulations. (a) Schematic of the wave packets in position space for initial polar angles $\theta = \pi/4$ (green), $\pi/2$ (orange), and $3\pi/4$ (pink). (b) Normalized rms width σ_z^* vs interaction strength χ at $t_d = 2\pi \times 30 / (|\chi_{\text{opt}}|N)$. The dashed lines indicate $\chi = \chi_{\text{opt}}(\pi/2)$. (c) Normalized rms width σ_z^* vs θ and χ at t_d . The red curve is the optimal interaction strength as given by Eq. (4). The cuts for $\theta = \pi/4, \pi/2, 3\pi/4$ are shown in panel (b).

defined by the optical cavity is important, since it enables resonant Raman coupling to four momentum states ($\pm\hbar k, \pm\hbar k$) all separated by $\omega_z = 2E_R + \omega_{\text{hf}}$ from $(0,0)$. Here, ω_{hf} is the energy splitting between $|\downarrow\rangle$ and another hyperfine level $|\uparrow\rangle$ —i.e., between the $F=2$ and $F=1$ ground hyperfine levels in ^{87}Rb atoms [inset of Fig. 4(a)]. Note that we added an additional internal degree of freedom to increase the energy difference ω_z by ω_{hf} , since in this case it is not boosted by a finite p_0 , as was the case in the 1D case.

After velocity selection, a follow-up Raman $\pi/2$ pulse can prepare an atom r in the array to the superposition state

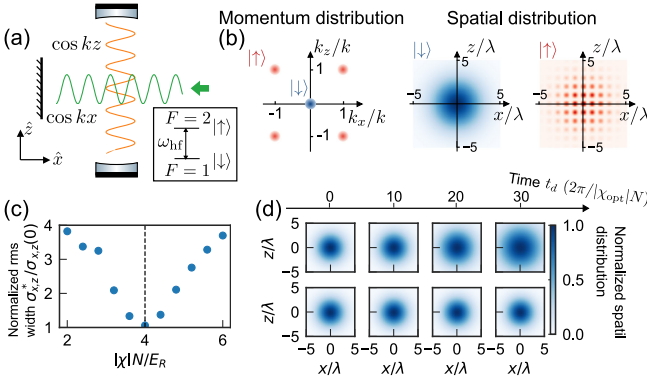


FIG. 4. Proposed scheme to stabilize a soliton in 2D. (a) It uses a standing-wave cavity along the z direction (orange) and a retroreflected drive field along the x direction (green). (b) The initial state is prepared via a Raman pulse as a superposition between $|0, 0; \downarrow\rangle$ and $|\pm\hbar k, \pm\hbar k; \uparrow\rangle$ in the 2D momentum-spin coupled basis. We plot the initial momentum and spatial distributions for the internal states $|\downarrow\rangle$ and $|\uparrow\rangle$. (c) Normalized rms width $\sigma_{x,z}^*$ for $|\downarrow\rangle$ vs χ at $t_d = 2\pi \times 100 / (|\chi_{\text{opt}}|N)$, with the optimal interaction strength given by $\chi_{\text{opt}} = -4E_R$. (d) Simulated spatial distribution vs time for $|\downarrow\rangle$. Top: $\chi = 0$; the wave packets broaden over time. Bottom: $\chi = \chi_{\text{opt}}$; the wave packets retain their initial shape without broadening.

$(1/\sqrt{2})(|\downarrow_{\vec{p}}\rangle_r + |\uparrow_{\vec{p}}\rangle_r)$ with $|\downarrow_{\vec{p}=(p_x, p_z)}\rangle_r \equiv |p_x, p_z, \downarrow\rangle_r$ and $|\uparrow_{\vec{p}}\rangle_r \equiv \frac{1}{2} \sum_{\mu_x, \mu_z = \pm 1} |p_x + \mu_x k, p_z + \mu_z k, \uparrow\rangle_r$, with the initial momentum and spatial distribution shown in Fig. 4(b).

Time evolution in the driven cavity enable processes in which an atom in $|\downarrow_{\vec{p}}\rangle$ absorbs a pump field photon (green), subsequently emitting a cavity photon (orange) while flipping the spin to $|\uparrow_{\vec{p}}\rangle$. The emitted photon is then absorbed by another $|\uparrow_{\vec{q}}\rangle$ atom, which then emits a green pump photon while flipping to $|\downarrow_{\vec{q}}\rangle$. As in the 1D case, these processes generate exchange interaction within the aforementioned spin-1/2 system. A similar type of process has been demonstrated in recent experiments [39,40].

In this situation again, one finds a modified energy spectrum similar to Eq. (2), but instead of $(2kp_r/M)^2$ one has $\sum_{\mu_x, \mu_z = \pm 1} [(kp_x/M)^2 + (kp_z/M)^2 + 2(k\mu_x p_x/M)(k\mu_z p_z/M)] = (2kp_x/M)^2 + (2kp_z/M)^2$. Therefore, again by choosing $N\chi_{\text{opt}} = -4E_R$, one can cancel the dispersion, but now in two directions [38].

In Fig. 4(c), we fit the position-space density of the $|\downarrow\rangle$ internal state using a 2D Gaussian function and plot the ratio of the rms width at $t_d = 2\pi \times 100 / (|\chi_{\text{opt}}|N)$, $\sigma_{x,z}^*$, to its initial width as a function of the interaction strength. In Fig. 4(d), we show the position-space density of the internal state $|\downarrow\rangle$ at different interaction times. For the noninteracting case ($\chi = 0$, top panel), the density profile broadens over time, whereas for the optimal interaction strength ($\chi = \chi_{\text{opt}}$, bottom panel), the initial shape is preserved. Interestingly, compared to the well-known self-organization transition [39,40], the exchange interaction preserves the Z_2 checkerboard pattern even when the transverse drive is weak.

A 3D soliton can be engineered in a similar way, but by replacing the transverse retroreflected beam along \hat{x} —i.e., perpendicular to the cavity by two orthogonal retroreflected beams now propagating along the $\hat{x} \pm \hat{y}$ directions, both again perpendicular to the cavity axis (see the End Matter).

Experimental considerations—In contrast to the narrow momentum distribution featured by a BEC, which can be imaged through time-of-flight measurements, a thermal gas presents the challenge of a much broader initial profile even after velocity selection [20]. This makes it difficult to experimentally observe the suppressed dispersion, as atoms will hit the lower-cavity mirror before they expand for sufficient observation time. For the 1D soliton, we propose a Raman interferometry scheme amenable to probing the emergent soliton in a thermal gas system with the details in Ref. [38]. The key idea is to use an additional external drive, instead of the exchange interactions, to prepare a soliton between a pair of momentum states in another hyperfine level $|0\rangle$, and inject it into one arm of the interferometer. We choose the cavity frequency to be far from resonant from the atomic transition for this internal state, to make it insensitive to exchange interactions. In the

other arm, we inject a soliton between another pair of momentum states in a hyperfine state $|1\rangle$ that experiences exchange interactions. We prepare an initial superposition of $|0\rangle$ and $|1\rangle$, thereby creating two types of solitons, and the contrast observed at the output of the interferometer is sensitive to the wave-packet spreading. This is different from the kinetic energy difference between the pseudospins, which generates interference fringes in the Bragg interferometer. This spectroscopic method could also be used to detect 2D and 3D solitons. In this case, however, it would be required to have access to four different internal levels, so the use of a BEC would make the detection easier.

Decoherence sources such as free-space scattering and superradiance from photons leaking out of the cavity, not included so far, can disrupt the coherence between momentum states and destroy the soliton [20], with the latter being the most relevant in large arrays. One way to mitigate superradiance, as discussed in the SM [38], is the use of a dual pump tone configuration [32,33], which enables the soliton to persist despite the finite photon lifetimes. The free-space scattering is over 2 orders of magnitude weaker than $\chi_{\text{opt}}N$ under current experimental conditions, and thus almost negligible [20].

Conclusion and outlook—We have proposed a scheme to manipulate atomic motion by leveraging the interplay between single-particle dispersion and many-body cavity interactions and providing a mechanism for generating solitons in 1D, 2D, and 3D geometries without quantum degeneracy. For thermal atoms, an interferometric detection protocol can be used to spectroscopically resolve the engineered dispersion [41]. Our Letter opens many different opportunities. In the context of quantum simulation, while contact interactions were neglected in our analysis, their inclusion could allow for the exploration of their enhanced role in flat-band systems. For quantum sensing, our system offers a resource both for miniaturized devices and for space-based inertial sensing enabled by 2D and 3D solitons. The solitons should enable longer interrogation times, favorable for tests of the weak equivalence principle in free-fall atoms, for instance, by detecting differential acceleration between isotopes. Finally, while most of the discussion was restricted to a mean-field analysis, beyond-mean-field effects can in addition generate spin squeezing for quantum-enhanced interferometry [31,35].

Acknowledgments—We thank Chitose Maruko and Yang Yang for useful feedback on the manuscript. This material is based upon work supported by the Vannevar Bush Faculty Fellowship, the Heising-Simons foundations, the NSF JILA-PFC PHY-2317149 and OMA-2016244 (QLCI), the U.S. Department of Energy, Office of Science, National Quantum Information Science Research Centers, Quantum Systems Accelerator, and NIST.

Data availability—The data that support the findings of this article are not publicly available upon publication because it is not technically feasible and/or the cost of preparing, depositing, and hosting the data would be prohibitive within the terms of this research project. The data are available from the authors upon reasonable request.

- [1] S. Burger, K. Bongs, S. Dettmer, W. Ertmer, K. Sengstock, A. Sanpera, G. V. Shlyapnikov, and M. Lewenstein, Dark solitons in Bose-Einstein condensates, *Phys. Rev. Lett.* **83**, 5198 (1999).
- [2] J. Denschlag, J. E. Simsarian, D. L. Feder, C. W. Clark, L. A. Collins, J. Cubizolles, L. Deng, E. W. Hagley, K. Helmerson, W. P. Reinhardt *et al.*, Generating solitons by phase engineering of a Bose-Einstein condensate, *Science* **287**, 97 (2000).
- [3] L. Khaykovich, F. Schreck, G. Ferrari, T. Bourdel, J. Cubizolles, L. D. Carr, Y. Castin, and C. Salomon, Formation of a matter-wave bright soliton, *Science* **296**, 1290 (2002).
- [4] K. E. Strecker, G. B. Partridge, A. G. Truscott, and R. G. Hulet, Formation and propagation of matter-wave soliton trains, *Nature (London)* **417**, 150 (2002).
- [5] B. Eiermann, T. Anker, M. Albiez, M. Taglieber, P. Treutlein, K.-P. Marzlin, and M. K. Oberthaler, Bright Bose-Einstein gap solitons of atoms with repulsive interaction, *Phys. Rev. Lett.* **92**, 230401 (2004).
- [6] B. Bakkali-Hassani, C. Maury, Y.-Q. Zou, E. Le Cerf, R. Saint-Jalm, P. C. M. Castilho, S. Nascimbene, J. Dalibard, and J. Beugnon, Realization of a Townes soliton in a two-component planar Bose gas, *Phys. Rev. Lett.* **127**, 023603 (2021).
- [7] C.-A. Chen and C.-L. Hung, Observation of scale invariance in two-dimensional matter-wave Townes solitons, *Phys. Rev. Lett.* **127**, 023604 (2021).
- [8] J. Polo and V. Ahufinger, Soliton-based matter-wave interferometer, *Phys. Rev. A* **88**, 053628 (2013).
- [9] J. Cuevas, P. Kevrekidis, B. Malomed, P. Dyke, and R. Hulet, Interactions of solitons with a Gaussian barrier: Splitting and recombination in quasi-one-dimensional and three-dimensional settings, *New J. Phys.* **15**, 063006 (2013).
- [10] J. L. Helm, S. L. Cornish, and S. A. Gardiner, Sagnac interferometry using bright matter-wave solitons, *Phys. Rev. Lett.* **114**, 134101 (2015).
- [11] C. L. Grimshaw, T. P. Billam, and S. A. Gardiner, Soliton interferometry with very narrow barriers obtained from spatially dependent dressed states, *Phys. Rev. Lett.* **129**, 040401 (2022).
- [12] J. L. Helm, T. P. Billam, and S. A. Gardiner, Bright matter-wave soliton collisions at narrow barriers, *Phys. Rev. A* **85**, 053621 (2012).
- [13] A. Marchant, T. Billam, T. Wiles, M. Yu, S. Gardiner, and S. Cornish, Controlled formation and reflection of a bright solitary matter-wave, *Nat. Commun.* **4**, 1865 (2013).
- [14] J. H. Nguyen, P. Dyke, D. Luo, B. A. Malomed, and R. G. Hulet, Collisions of matter-wave solitons, *Nat. Phys.* **10**, 918 (2014).
- [15] G. D. McDonald, C. C. N. Kuhn, K. S. Hardman, S. Bennetts, P. J. Everitt, P. A. Altin, J. E. Debs, J. D. Close,

- and N. P. Robins, Bright solitonic matter-wave interferometer, *Phys. Rev. Lett.* **113**, 013002 (2014).
- [16] A. M. Rey, L. Jiang, M. Fleischhauer, E. Demler, and M. D. Lukin, Many-body protected entanglement generation in interacting spin systems, *Phys. Rev. A* **77**, 052305 (2008).
- [17] C. Deutsch, F. Ramirez-Martinez, C. Lacroûte, F. Reinhard, T. Schneider, J.-N. Fuchs, F. Piéchon, F. Laloë, J. Reichel, and P. Rosenbusch, Spin self-rephasing and very long coherence times in a trapped atomic ensemble, *Phys. Rev. Lett.* **105**, 020401 (2010).
- [18] M. A. Norcia, R. J. Lewis-Swan, J. R. Cline, B. Zhu, A. M. Rey, and J. K. Thompson, Cavity-mediated collective spin-exchange interactions in a strontium superradiant laser, *Science* **361**, 259 (2018).
- [19] S. Smale, P. He, B. A. Olsen, K. G. Jackson, H. Sharum, S. Trotzky, J. Marino, A. M. Rey, and J. H. Thywissen, Observation of a transition between dynamical phases in a quantum degenerate Fermi gas, *Sci. Adv.* **5**, eaax1568 (2019).
- [20] C. Luo, H. Zhang, V. P. Koh, J. D. Wilson, A. Chu, M. J. Holland, A. M. Rey, and J. K. Thompson, Momentum-exchange interactions in a Bragg atom interferometer suppress Doppler dephasing, *Science* **384**, 551 (2024).
- [21] Z. Niu, V. M. Schäfer, H. Zhang, C. Wagner, N. R. Taylor, D. J. Young, E. Y. Song, A. Chu, A. M. Rey, and J. K. Thompson, Many-body gap protection against motional dephasing of an optical clock transition, *Phys. Rev. Lett.* **134**, 113403 (2025).
- [22] R. J. Lewis-Swan, D. Barberena, J. R. K. Cline, D. J. Young, J. K. Thompson, and A. M. Rey, Cavity-QED quantum simulator of dynamical phases of a Bardeen-Cooper-Schrieffer superconductor, *Phys. Rev. Lett.* **126**, 173601 (2021).
- [23] D. J. Young, A. Chu, E. Y. Song, D. Barberena, D. Wellnitz, Z. Niu, V. M. Schäfer, R. J. Lewis-Swan, A. M. Rey, and J. K. Thompson, Observing dynamical phases of BCS superconductors in a cavity QED simulator, *Nature (London)* **625**, 679 (2024).
- [24] D. J. Young, E. Y. Song, A. Chu, D. Barberena, Z. Niu, V. M. Schäfer, R. J. Lewis-Swan, A. M. Rey, and J. K. Thompson, Time-resolved pairing gap spectroscopy in a quantum simulator of fermionic superfluidity inside an optical cavity, *arXiv:2408.12640*.
- [25] J. Dalibard, F. Gerbier, G. Juzeliūnas, and P. Öhberg, Colloquium: Artificial gauge potentials for neutral atoms, *Rev. Mod. Phys.* **83**, 1523 (2011).
- [26] Y.-J. Lin, K. Jiménez-García, and I. B. Spielman, Spin-orbit-coupled Bose-Einstein condensates, *Nature (London)* **471**, 83 (2011).
- [27] P. Wang, Z.-Q. Yu, Z. Fu, J. Miao, L. Huang, S. Chai, H. Zhai, and J. Zhang, Spin-orbit coupled degenerate Fermi gases, *Phys. Rev. Lett.* **109**, 095301 (2012).
- [28] L. Huang, Z. Meng, P. Wang, P. Peng, S.-L. Zhang, L. Chen, D. Li, Q. Zhou, and J. Zhang, Experimental realization of two-dimensional synthetic spin-orbit coupling in ultracold fermi gases, *Nat. Phys.* **12**, 540 (2016).
- [29] H. Sakaguchi, B. Li, and B. A. Malomed, Creation of two-dimensional composite solitons in spin-orbit-coupled self-attractive Bose-Einstein condensates in free space, *Phys. Rev. E* **89**, 032920 (2014).
- [30] Y.-C. Zhang, Z.-W. Zhou, B. A. Malomed, and H. Pu, Stable solitons in three dimensional free space without the ground state: Self-trapped Bose-Einstein condensates with spin-orbit coupling, *Phys. Rev. Lett.* **115**, 253902 (2015).
- [31] G. P. Greve, C. Luo, B. Wu, and J. K. Thompson, Entanglement-enhanced matter-wave interferometry in a high-finesse cavity, *Nature (London)* **610**, 472 (2022).
- [32] C. Luo, H. Zhang, A. Chu, C. Maruko, A. M. Rey, and J. K. Thompson, Hamiltonian engineering of collective XYZ spin models in an optical cavity, *Nat. Phys.* **21**, 916 (2025).
- [33] C. Luo, H. Zhang, C. Maruko, E. A. Bohr, A. Chu, A. M. Rey, and J. K. Thompson, Realization of three and four-body interactions between momentum states in a cavity through optical dressing, *arXiv:2410.12132*.
- [34] A. Shankar, L. Salvi, M. L. Chiofalo, N. Poli, and M. J. Holland, Squeezed state metrology with Bragg interferometers operating in a cavity, *Quantum Sci. Technol.* **4**, 045010 (2019).
- [35] J. D. Wilson, J. T. Reilly, H. Zhang, C. Luo, A. Chu, J. K. Thompson, A. M. Rey, and M. J. Holland, Entangled matter waves for quantum enhanced sensing, *Phys. Rev. A* **110**, L041301 (2024).
- [36] R. Gerritsma, G. Kirchmair, F. Zähringer, E. Solano, R. Blatt, and C. Roos, Quantum simulation of the Dirac equation, *Nature (London)* **463**, 68 (2010).
- [37] L. J. LeBlanc, M. Beeler, K. Jimenez-Garcia, A. R. Perry, S. Sugawa, R. Williams, and I. B. Spielman, Direct observation of zitterbewegung in a Bose-Einstein condensate, *New J. Phys.* **15**, 073011 (2013).
- [38] See Supplemental Material at <http://link.aps.org/supplemental/10.1103/qrk6-phhk> for details of the theoretical model, and derivations supporting the results presented in the main text, includes Refs. [18,20,32,33].
- [39] K. Baumann, C. Guerlin, F. Brennecke, and T. Esslinger, Dicke quantum phase transition with a superfluid gas in an optical cavity, *Nature (London)* **464**, 1301 (2010).
- [40] F. Mivehvar, F. Piazza, T. Donner, and H. Ritsch, Cavity QED with quantum gases: New paradigms in many-body physics, *Adv. Phys.* **70**, 1 (2021).
- [41] L. Balents, C. R. Dean, D. K. Efetov, and A. F. Young, Superconductivity and strong correlations in moiré flat bands, *Nat. Phys.* **16**, 725 (2020).

End Matter

Solitons in higher dimensions—In this section, we discuss a protocol for generating two-dimensional solitons. It uses concepts similar to those discussed previously, but with the necessary modifications to address the challenges of higher-dimensional systems.

To notice such challenges, imagine we couple two momentum states (p_x, p_z) and $(p_x + \hbar k_x, p_z + \hbar k_z)$ through the cavity by exchanging photons with a wave vector (k_x, k_z) . The resulting effective dispersion becomes

$$\begin{aligned}
 E_{\vec{p}=(p_x,p_z)} &= -\frac{1}{2}\sqrt{(\chi N)^2 + \left(\frac{k_x p_x + k_z p_z}{M}\right)^2} + \frac{p_x^2 + p_z^2}{2M\hbar} \\
 &\approx \frac{\chi N}{2} + \frac{p_x^2}{2M\hbar} \left(1 + \frac{\hbar k_x^2}{2M\chi N}\right) \\
 &\quad + \frac{p_z^2}{2M\hbar} \left(1 + \frac{\hbar k_z^2}{2M\chi N}\right) + \frac{p_x p_z k_x k_z}{2M^2 \chi N}. \quad (\text{A1})
 \end{aligned}$$

The cross term proportional to $p_x p_z$ cannot be canceled, resulting in an anisotropic dispersion that broadens the wave packets instead of a soliton.

We propose an alternative scheme to form a 2D soliton via the superposition of five momentum states centered around $(0,0)$ and $(\pm\hbar k, \pm\hbar k)$. The main idea behind this is the use of an additional retroreflected beam perpendicular to the cavity direction, which creates a standing wave spatial profile $\propto \cos(kx)\cos(ky)$ as discussed in the main text, and an additional internal state degree of freedom, labeled $|\uparrow\rangle$ and $|\downarrow\rangle$. The internal levels are separated by an energy splitting ω_{hf} . This setting is closely related to the well-known self-organization transition broadly explored in cold gases [39,40]. Following Ref. [40], the effective Hamiltonian in the far detuned limit corresponds to an LMG model: $\hat{H}_{\text{LMG}} + \hat{H}_{\text{dis}}$, with $\hat{H}_{\text{LMG}} = \omega_Z \hat{S}_Z + \omega_Z \hat{S}_Z + \chi \hat{S}_X^2$ when written in terms of the spin-momentum states $|\downarrow_{\vec{p}}\rangle \equiv |\vec{p}, \downarrow\rangle_r = (\hat{\psi}_{\vec{p}}^\downarrow)^\dagger |0\rangle$ and $|\uparrow_{\vec{p}}\rangle_r = \frac{1}{2} \sum_{\mu_x, \mu_z = \pm} |\uparrow_{\vec{p}, \mu_x, \mu_z}\rangle_r$ with $|\uparrow_{\vec{p}, \mu_x, \mu_z}\rangle_r \equiv |p_x + \mu_x \hbar k, p_z + \mu_z \hbar k, \uparrow\rangle_r = (\hat{\psi}_{\vec{p}, \mu_x, \mu_z}^\uparrow)^\dagger |0\rangle$. The density operators are defined as $\hat{n}_{\vec{p}, r}^\downarrow = (\hat{\psi}_{\vec{p}, r}^\downarrow)^\dagger \hat{\psi}_{\vec{p}, r}^\downarrow$, $\hat{n}_{\vec{p}, \mu_x, \mu_z}^\uparrow = (\hat{\psi}_{\vec{p}, \mu_x, \mu_z}^\uparrow)^\dagger \hat{\psi}_{\vec{p}, \mu_x, \mu_z}^\uparrow$ and the identity operator is defined as $\hat{I}_{\vec{p}, r} = \hat{n}_{\vec{p}, r}^\downarrow + \sum_{\mu_x, \mu_z = \pm} \hat{n}_{\vec{p}, \mu_x, \mu_z}^\uparrow$.

The single-particle kinetic Hamiltonian reads

$$\begin{aligned}
 \hat{H}_{\text{dis}} &= \sum_r \frac{p_{x,r}^2 + p_{z,r}^2}{2M} \hat{n}_{\vec{p}, r}^\downarrow \\
 &\quad + \sum_{r, \mu_x, \mu_z} \left(\omega_{\text{hf}} + \frac{(p_{x,r} + \mu_x \hbar k)^2 + (p_{z,r} + \mu_z \hbar k)^2}{2M} \right) \hat{n}_{\vec{p}, \mu_x, \mu_z}^\uparrow \\
 &= \sum_r \frac{p_{x,r}^2 + p_{z,r}^2}{2M} \hat{I}_{\vec{p}, r} \\
 &\quad + \sum_{r, \mu_x, \mu_z} \left(\omega_\chi + \frac{\mu_x \hbar k p_{x,r} + \mu_z \hbar k p_{z,r}}{M} \right) \hat{n}_{\vec{p}, \mu_x, \mu_z}^\uparrow, \quad (\text{A2})
 \end{aligned}$$

Notice that above, we take the large pump-cavity detuning and weak pump field limit to ignore the extra lattice trapping potential due to the ac Stark shift from either cavity or pump field [39].

To generate the desired exchange interactions, one needs $\chi N \ll \omega_Z$. Unlike the 1D case, here the momentum boost p_0 is absent, significantly reducing the average kinetic energy difference to $2E_R$. But the additional

internal-state energy difference can come to the rescue (this is why we needed another internal state), making the average energy difference between the states $\omega_Z = \omega_{\text{hf}} + 2E_R$. If $\chi N \ll \omega_Z$, then terms that do not preserve the total magnetization are rotated out, thus restoring the interacting part of the Hamiltonian to an exchange interacting model:

$$\begin{aligned}
 \hat{H}_{\text{ex}} &= \chi \sum_{n,m} (\hat{\psi}_{\vec{p}_n}^\uparrow)^\dagger \hat{\psi}_{\vec{p}_n}^\downarrow (\hat{\psi}_{\vec{p}_m}^\downarrow)^\dagger \hat{\psi}_{\vec{p}_m}^\uparrow \\
 &\approx \frac{\chi N}{2} \sum_n \left[(\hat{\psi}_{\vec{p}_n}^\uparrow)^\dagger \hat{\psi}_{\vec{p}_n}^\downarrow + (\hat{\psi}_{\vec{p}_n}^\downarrow)^\dagger \hat{\psi}_{\vec{p}_n}^\uparrow \right]. \quad (\text{A3})
 \end{aligned}$$

For convenience, we define another complete set of orthogonal states, starting from the symmetric superposition $|\uparrow_{\vec{p}}\rangle_r$. The other three orthogonal dressed states are given by

$$\begin{aligned}
 |\uparrow_{\vec{p}, A_1}\rangle_r &= \frac{1}{2} \left(|\uparrow_{\vec{p}, ++}\rangle_r + |\uparrow_{\vec{p}, +-}\rangle_r - |\uparrow_{\vec{p}, -+}\rangle_r - |\uparrow_{\vec{p}, --}\rangle_r \right), \\
 |\uparrow_{\vec{p}, A_2}\rangle_r &= \frac{1}{2} \left(|\uparrow_{\vec{p}, ++}\rangle_r - |\uparrow_{\vec{p}, +-}\rangle_r + |\uparrow_{\vec{p}, -+}\rangle_r - |\uparrow_{\vec{p}, --}\rangle_r \right), \\
 |\uparrow_{\vec{p}, A_3}\rangle_r &= \frac{1}{2} \left(|\uparrow_{\vec{p}, ++}\rangle_r - |\uparrow_{\vec{p}, +-}\rangle_r - |\uparrow_{\vec{p}, -+}\rangle_r + |\uparrow_{\vec{p}, --}\rangle_r \right). \quad (\text{A4})
 \end{aligned}$$

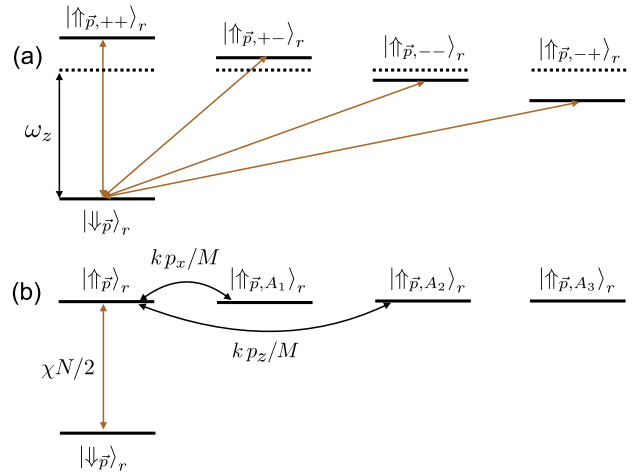


FIG. 5. Mean-field coupling diagram in 2D for atom r . (a) The system consists of five states in the bare basis: $|\downarrow_{\vec{p}}\rangle \equiv |\vec{p}, \downarrow\rangle_r$ and four momentum states $|\uparrow_{\vec{p}, \mu_x, \mu_z}\rangle_r \equiv |p_x + \mu_x \hbar k, p_z + \mu_z \hbar k, \uparrow\rangle_r$ with $\mu_x, \mu_z = \pm$. The single-particle energy difference between them is given by $\omega_Z + (p_x \mu_x \hbar k + p_z \mu_z \hbar k)/M$. The exchange interaction (orange arrows) couples $|\downarrow_{\vec{p}}\rangle_r$ to all four momentum states $|\uparrow_{\vec{p}, \mu_x, \mu_z}\rangle_r$. (b) Since the exchange interaction only couples $|\downarrow_{\vec{p}}\rangle_r$ to the symmetric superposition of the four momentum states $|\uparrow_{\vec{p}}\rangle_r$, it is convenient to use a different basis, defined in Eq. (A4). In this basis, the single-particle inhomogeneity is no longer diagonal and has couplings between the states, $|\uparrow_{\vec{p}, A_1}\rangle_r$ and $|\uparrow_{\vec{p}, A_2}\rangle_r$, with strengths $k p_x / M$ and $k p_z / M$, respectively.

In this basis, the matrix that governs the dynamics of the atoms is given by [Figs. 5(a) and 5(b)]: $\{|\downarrow_{\vec{p}}\rangle_r, |\uparrow_{\vec{p}}\rangle_r, |\uparrow_{\vec{p},A_1}\rangle_r, |\uparrow_{\vec{p},A_2}\rangle_r, |\uparrow_{\vec{p},A_3}\rangle_r\}$ is given by

$$\begin{pmatrix} 0 & \frac{\chi N}{2} & 0 & 0 & 0 \\ \frac{\chi N}{2} & 0 & \frac{kp_x}{M} & \frac{kp_z}{M} & 0 \\ 0 & \frac{kp_x}{M} & 0 & 0 & 0 \\ 0 & \frac{kp_z}{M} & 0 & 0 & 0 \\ 0 & 0 & 0 & 0 & 0 \end{pmatrix}. \quad (\text{A5})$$

When a $\pi/2$ Raman pulse is applied—generated via a two-photon Raman transition by pumping both the cavity and a transverse field— $(1/\sqrt{2})(|\downarrow_{\vec{p}}\rangle_r + |\uparrow_{\vec{p}}\rangle_r)$ one in fact prepares a state that has substantial overlap with an eigenstate of the matrix above with an eigenenergy

$$\begin{aligned} E_{\vec{p}} &= -\sqrt{\left(\frac{\chi N}{2}\right)^2 + \left(\frac{kp_x}{M}\right)^2 + \left(\frac{kp_z}{M}\right)^2} + \frac{p_x^2 + p_z^2}{2M\hbar} \\ &\approx \frac{\chi N}{2} + \left(1 + \frac{4E_R}{\chi N}\right) \frac{p_x^2 + p_z^2}{2M\hbar}. \end{aligned} \quad (\text{A6})$$

Now, similarly to the 1D scenario, by choosing the interaction strength to be $\chi_{\text{opt}}N = -4E_R$, one can remove the dispersion at the leading order, enabling the formation of a stable 2D soliton.

A 3D soliton can also be stabilized using the setup shown in Fig. 6(a). Here, we have the cavity field along the z

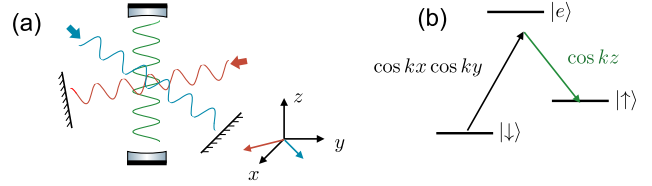


FIG. 6. (a) Proposed scheme to stabilize a soliton in 3D, using a standing-wave cavity along the z direction (green) and two retroreflected drive fields along the $x \pm y$ directions (red and blue). (b) Cavity-assist two-photon transition between the $|\uparrow\rangle$ and $|\downarrow\rangle$ internal states with a spatial profile $\propto \cos kx \cos ky \cos kz$.

(green) direction and two transverse retroreflected beams along the $x \pm y$ directions (blue and red). These two fields create an interference pattern with a spatial profile $\propto \cos(kx + ky) + \cos(kx - ky) = 2 \cos kx \cos ky$. Using them, a Raman pulse can be used to prepare, via a two-photon transition, an initial state that is a coherent superposition between $|0, 0, 0, \downarrow\rangle$ and $|\pm\hbar k, \pm\hbar k, \pm\hbar k, \downarrow\rangle$, as shown in Fig. 6(b). In this system, the exchange interaction is generated by exchanging photons in the cavity as follows: an atom in $|\downarrow_{\vec{p}}\rangle$ absorbs a pump field photon with spatial profile $\propto \cos kx \cos ky$, subsequently emitting a cavity photon (green) and flipping the spin to $|\uparrow_{\vec{p}}\rangle$. The emitted photon is then absorbed by another atom in state $|\uparrow_{\vec{q}}\rangle$, which emits a pump photon while flipping its state to $|\downarrow_{\vec{q}}\rangle$. A similar analysis to the one discussed for the 2D case is also applicable here, resulting in the same optimal interaction strength, $\chi_{\text{opt}}N = -4E_R$.